Precipitation driving of droplet concentration variability in marine low clouds

***Robert Wood[1], David Leon[2], Matthew Lebsock[3], Jefferson Snider[2], Antony D. Clarke[4]**

1. Department of Atmospheric Sciences, 408 ATG Building, University of Washington, Seattle, WA, 98195-1640, USA.

2. Department of Atmospheric Sciences, University of Wyoming, Dept. 3038 1000 E. University Ave., Laramie, WY 82071, USA

3. Jet Propulsion Laboratory, California Institute of Technology, 4800 Oak Grove Drive, Pasadena, California 91109-8099, USA

4. Department of Oceanography, University of Hawai`i at Manoa, 1000 Pope Road, Marine Sciences Building, Honolulu, HI 96822, USA

* Corresponding author (robwood@atmos.washington.edu

Tel: 206-543-1203; Fax: +1 206 685 9302)

June 14th 2012

Abstract

The concentration N_d of cloud droplets in marine low clouds is a primary determinant of their ability to reflect sunlight and modulates their ability to precipitate. Previous studies have focused upon aerosol source variability as the key driver of variability in N_d. Here, we use a highly simplified aerosol budget model to examine the impact of precipitation on N_d. This model considers: precipitation (coalescence) scavenging, constrained using new satellite measurements of light precipitation; entrainment of aerosol from above cloud combined with constant aerosol concentration based on recent field observations of aerosol particles in the free troposphere; and sea-surface aerosol production estimated using a wind-speed dependent source function. Despite the highly simplified nature of this model, it skillfully predicts the geographical variability of N_d in regions of extensive marine low clouds. Inclusion of precipitation results in reduction in N_d by factors of 2-3 over the remote oceans. Near the coastline the reduction in N_d due to precipitation is ~15%, however the model is not able to accurately predict N_d close to the coastline due to strong pollution sources. Surface CCN sources alone are insufficient to maintain N_d against precipitation losses. These results demonstrate that even the light precipitation rates typical of marine stratocumulus profoundly impact the radiative properties of marine low clouds.

1. Introduction

Anthropogenic activities have resulted in marked increases in the concentration of aerosol particles in the atmosphere [*Kaufman et al.* 2002, *Isaksen et al.* 2009] and these increases exert a significant but highly uncertain radiative forcing on the global climate [*Isaksen et al*. 2009, *IPCC* 2007]. A large fraction of this forcing is attributed to the effects that aerosol particles have on clouds by increasing the concentration N_d of cloud droplets [*Martin et al.* 1994; *Ramanathan et al*. 2001; *Lohmann and Feichter* 2005], reducing droplet size [*Breon et al. 2002*], thereby increasing the reflected solar radiation [*Twomey* 1974, *Penner et al.* 2004, *Quaas et al.* 2009]. Systematic increases in N_d have been observed downwind of east Asia over the past two decades [*Bennartz et al*., 2011] and have been attributed to rapid industrialization. The magnitude of the so-called "aerosol indirect effect" on climate depends not only upon present-day conditions, but also upon the unperturbed microphysical state of the clouds prior to the addition of anthropogenic aerosols [*Platnick and Twomey* 1994, *Oreopoulos and Platnick*, 2008]. It is reasonable to argue that N_d is the single most important cloud microphysical variable that must be accurately represented in models in order to accurately determine aerosol indirect effects on climate. However, there are marked differences between values of N_d in different climate models [*Quaas et al.* 2009, *Ming et al.* 2006, *Gettelman et al.* 2008] demonstrating a clear lack of understanding of the key controls on N_d.

Satellite-based studies use the relationship between observed cloud droplet size or concentration, and nearby clear-sky estimates of aerosol loading, to infer the role that aerosols play in influencing clouds and climate [*Breon et al.* 2002]. Some even go so far as to quantitatively estimate aerosol indirect effects globally [*Quaas et al.* 2008, *Jones et*

70 *al.* 2009]. Inherent in this approach is that correlations between cloud microphysical
71 properties and aerosols in the current climate are indicative of an aerosol influence on
72 cloud properties rather than vice versa. Aerosol-cloud correlative studies do not take the
73 possible effects of precipitation into account. One can make a reasonable case that
74 precipitation-induced aerosol changes will not significantly impact the inferences drawn
75 from these studies only if one assumes that the impacts of precipitation are localized,
76 intermittent, and relatively rare, and that the aerosol fields that interact with the majority
77 of clouds are not significantly affected by precipitation. However, recent observations
78 from the sensitive spaceborne radar on the CloudSat satellite are finding that precipitation
79 occurs more frequently over the globe than previously thought [*Leon et al.* 2008, *Haynes*
80 *et al.* 2009] prompting an examination of the role of precipitation in driving aerosol
81 variability.

82 In this study we use these state-of-the-art quantitative estimates of light
83 precipitation from CloudSat to constrain a simple budget model that predicts the mean
84 concentrations of cloud condensation nuclei (CCN) and cloud droplets over those parts of
85 the global oceans containing extensive low clouds. These clouds are confined within the
86 marine boundary layer (MBL) and are among the most susceptible to aerosol
87 perturbations [*Oreopoulos and Platnick*, 2008]. We build upon previous studies [*Baker*
88 *and Charlson* 1990, *Baker et al.* 1993] that used simplified budget models to provide
89 important insights into the factors controlling CCN, by constructing a steady-state budget
90 for CCN in the MBL appropriate for the regions of large-scale subsidence where
91 extensive marine stratocumulus clouds are favored [*Klein and Hartmann*, 1993].

This article is organized as follows. Section 2 describes the basis for a simple, single-equation, steady-state budget model to predict CCN/N_d in the MBL. Section 3 describes how we determine the terms in the budget using a variety of observations including satellites and in-situ data. Section 4 presents the key results from the model and compares the model against satellite observations of N_d. Section 5 discusses the implications of our findings.

2. Steady state budget model

The rate of increase of CCN concentration $\dot{N}$ averaged over the depth of the MBL can be written as the sum of various source and sink terms:

$$\dot{N} = \dot{N}_{FT} + \dot{N}_S + \dot{N}_P + \dot{N}_{DRY} + \dot{N}_{ADV} \quad [1]$$

where $\dot{N}_{FT}$, $\dot{N}_S$, $\dot{N}_P$, $\dot{N}_{DRY}$, and $\dot{N}_{ADV}$ are the time tendencies due to entrainment of CCN from the free-troposphere (FT), primary production at the surface (i.e. sea spray), precipitation (i.e. coalescence scavenging), dry deposition to the surface, and horizontal advection respectively.

Free-tropospheric air is constantly being mixed into the MBL by cloud top entrainment, and this can either provide a net source of CCN to the MBL or can dilute MBL aerosol concentrations. Modeling and observational studies suggest that the FT is a primary source of CCN in the remote MBL [*Clarke et al.* 1998b, *Capaldo et al.* 1999, *Katoshevski et al*. 1999]. The net source rate is $\dot{N}_{FT} = w_e(N_{FT}–N)/z_i$ where z_i is the depth of the MBL and w_e is the entrainment rate.

The modeled surface source $\dot{N}_S$ is assumed to be from primary production of sea-spray aerosol (SSA) and we use a recent parameterization [*Clarke et al.* 2006] to provide

$\dot{N}_S = F(\sigma) U_{10}^{3.41} / z_i$ where U_{10} is the wind speed at a height of 10 m, and $F(\sigma)$ depends upon the assumed peak supersaturation σ experienced in the clouds (see section 2.2 below). We examine the sensitivity to the parameterization of sea-spray by comparing with the frequently-used formulation of *Monahan et al.* [1986]. Since this formulation has the same wind speed dependence as *Clarke et al.* [2006], the expression for $\dot{N}_S$ given above is identical for the two schemes, but the function $F(\sigma)$is different. We discuss how the supersaturation and $F(\sigma)$ are specified in Sections 3.1 and 3.3 below.

The model does not take into account CCN formation from the nucleation of new particles in the MBL since it is unlikely that this contributes significantly to the mean CCN number concentration over the oceans. In severely-scavenged ultraclean MBLs evidence of new particle formation has been noted [*Clarke et al.* 1998, *Petters et al.* 2006, *Tomlinson et al.* 2007, *Wood et al.* 2008] . Such nucleation events appear to be quite rare, with only one clear instance observed during four weeks of shipborne sampling over the tropical southeastern Pacific ocean [*Tomlinson et al.* 2007]. In addition, evidence that freshly nucleated particles can grow to sufficient sizes to increase the population of CCN without being scavenged by existing cloud is lacking. Nucleation events are therefore unlikely to compete with other source processes in determining the mean state [*Capaldo et al.* 1999, *Katoshevski et al*. 1999]. In any case, formulations for the rate of production of CCN from new particle formation in the MBL are highly uncertain [*Capaldo et al.* 1999, *Kirkby et al.* 2011].

The precipitation sink term $\dot{N}_P$ depends upon the precipitation rate at cloud base P_{CB}. We use a formulation which accounts for losses from the collection of cloud droplets by precipitation drops in the cloud via accretion [*Wood* 2006]. This gives $\dot{N}_P = K$

$N P_{CB} h/z_i$, where $K = 2.25$ m^2 kg^{-1} is a constant that depends upon the collection efficiency of cloud droplets by drizzle drops [*Wood* 2006], and h is the cloud thickness.

Dry deposition of CCN to the ocean is estimated using deposition velocity parameterization [*Georgi* 1988] for accumulation mode particles (0.05-1 μm diameter) which make up the bulk of the CCN in the MBL. Rates are in the range 0.001-0.01 cm s^{-1} with the higher values occurring at higher wind speeds and for the larger of the accumulation mode particles. Given these deposition velocities, we find that dry deposition constitutes only a very weak sink for CCN under most circumstances, with loss rates unlikely to exceed 2 cm^{-3} d^{-1} for most values of N observed, and most wind speeds, over the oceans. We are therefore justified in setting $\dot{N}_{DRY} = 0$ in the budget model.

We also set $\dot{N}_{ADV} = 0$ to avoid the complication of calculating spatial gradients and to facilitate the interpretation of the key physical processes controlling N_d. It is possible to estimate the magnitude of the advection term $\dot{N}_{ADV}$ using the observed cloud droplet concentration from satellite [*George and Wood* 2010]. Over the remote oceans the magnitude of $\dot{N}_{ADV}$ is generally 10 cm^{-3} d^{-1} or less, while higher values can be found in near-coastal regions. Including advection in the steady state model introduces an additional level of complexity since it involves taking spatial gradients. To preserve simplicity we omit it from the model. Since precipitation is the dominant control on N_d in the model, the geographic pattern of the advection term largely follows the spatial gradient in precipitation rate.

In this study we examine the time-mean CCN budget by setting $\dot{N}$=0 in equation (1) inserting the expressions discussed above for the various terms, and

rearranging to obtain an expression for the steady-state value N_{eq} of the CCN concentration in the MBL as

$$N_{eq} = \frac{\left(N_{FT} + \frac{F(\sigma)U_{10}^{3.41}}{Dz_i}\right)}{\left(1 + \frac{hKP_{CB}}{Dz_i}\right)} \quad [2]$$

Here we have also assumed that entrainment is in balance with the large-scale subsidence rate, so that $w_e = D\, z_i$, where D is the large scale divergence, appropriately assumed to be constant with height over the depth of the MBL [*Wood et al.* 2009]. In practice, the entrainment rate exceeds the subsidence rate by 10-40% over the subtropical stratocumulus regions [*Wood and Bretherton* 2004], but estimating its precise value is itself a major challenge [*Stevens* 2002] and is not attempted here.

3. Model constraints and inputs

The CCN budget model (equations 1 and 2) implicitly assumes that the cloud droplet concentration N_d and the CCN concentration are one and the same. This is reasonable provided that (a) we choose an appropriate peak supersaturation σ in order to convert the aerosol sources, which are provided as a function of aerosol size, into tendencies of CCN; (b) the cloud droplet concentration throughout the cloud is equal to that determined by the aerosol activation process.

181 3.1 Supersaturation

182 For marine stratocumulus clouds, observations suggest that values of σ in the
183 range 0.1-0.8% are typical with mean values around 0.3% consistent with observations
184 [*Martin et al.* 1994, *Snider et al.* 2003]. Here we assume a constant value of σ=0.3% for
185 all calculations. The peak supersaturation σ = 0.3% assumed in the model is assumed to
186 be constant everywhere. Understanding how this changes systematically over the remote
187 oceans is complex, as it depends upon variations in the strength of the turbulent updrafts
188 and upon the size distribution of the aerosol being activated [*Martin et al.* 1994, *Snider et*
189 *al.* 2003]. We use recent field measurements of mean aerosol size distributions at
190 different distances from the Chilean coast from the VOCALS Regional Experiment
191 (REx) [*Wood et al.* 2011] to estimate the likely systematic geographical variability in σ.
192 In the marine boundary layer, the Hoppel minimum [*Hoppel* 1986] in the size distribution
193 is indicative of the minimum size of aerosols that are activated. Assuming a hygroscopic
194 aerosol, this minimum size is directly related to the supersaturation. A systematic
195 reduction from 0.1 to 0.07 μm in the minimum diameter was observed to occur from
196 70°W to 78°W moving westwards along 20°S away from the Chilean coast [*Kleinmann*
197 *et al.* 2012]. This implies that the mean supersaturation increases by ~75% from the coast
198 offshore. However, the coastal CCN concentrations are high consistent with pollution
199 aerosol impacts [*Allen et al.* 2011], and so these are not representative of the
200 supersaturations we are attempting to represent in the model. No systematic shift in the
201 Hoppel minimum is observed over the cleaner region from 74°W to 78°W, suggesting
202 that systematic changes in supersaturation over the remoter regions may be considerably
203 smaller than occur near the coasts.

204 3.2 Free-tropospheric CCN

205 We constrain N_{FT} based on aerosol measurements from field data taken in the
206 Southern and Northern Hemisphere remote subtropical FT. Two data sources are used:
207 (a) aircraft measurements of FT CCN from a thermal diffusion CCN counter taken on
208 the NSF/NCAR C-130 aircraft during the VOCALS-REx. Details of the
209 instrument are provided in *Snider et al.* (2006), and flight plans are described in
210 *Wood et al.* [2011] A total of 638 CCN measurements were made in the FT (61,
211 117, 147 and 313 at supersaturations of approximately 0.1, 0.25, 0.5 and 0.9%
212 respectively) along the 20°S latitude line from the coast (70°W) to approximately
213 1500 km offshore (85°W) over the month-long campaign. CCN concentrations
214 are corrected to an assumed mean MBL pressure of 925 hPa, which is the typical
215 pressure at which clouds form in the region [*Bretherton et al*. 2010];
216 (b) a composite time-mean size distribution measured over 17 days with large scale
217 subsidence at a remote FT station on Mauna Loa during July 1992. These data are
218 described in *Weber and McMurry* [1996] and are also corrected to a pressure of
219 925 hPa. We convert the size distribution into a CCN spectrum using a plausible
220 range of aerosol hygroscopicity following the 'kappa' parameter approach
221 [*Petters and Kreidenweis* 2007]. A reasonable lower boundary (κ=0.3) is
222 approximately the lowest value of CCN-based hygroscopicity measured in the
223 northeastern Pacific FT from *Roberts et al.* (2010). The upper boundary (κ=0.98)
224 is the geometric mean value from *Roberts et al.* (2010). Values of κ significantly
225 higher than unity were inferred from CCN measurements in Roberts et al. (2010)
226 but seem implausible given that even the most hygroscopic compounds have κ

values of about unity [*Petters and Kreidenweis* 2007]. Ammonium sulfate has a κ value of approximately 0.7 [*Petters and Kreidenweis* 2007].

Figure 1 compares the measured CCN concentrations in the southeastern Pacific FT with those from Mauna Loa. For the southeastern Pacific, we take data from west of 75°W (>500 km off the Chilean coast) that is minimally impacted by coastal pollution [*Allen et al.* 2010]. Time-mean CCN concentrations west of 75°W over the southeastern Pacific Ocean (Fig. 1) are in remarkably good agreement with those derived from the Mauna Loa size distribution measurements. This is perhaps surprising because although the southeastern Pacific and Hawaii are in similar tropical meteorological regimes, one might expect marked differences in the mean size distribution due to the different array of sources and landmasses in the Northern and Southern Hemisphere. The mean distributions are made up of a mixture of different aerosol populations from a number of different sources. Previous studies [*Clarke et al.* 1998b, *Friedlander* 1977, *Raes* 1995] suggest that new particle formation from naturally-produced sulfuric acid in the upper troposphere constitutes one major source of clean FT CCN. This aerosol subsequently subsides in the descending branches of large scale atmospheric systems where its distribution is expected to reach a quasi-steady state [*Friedlander* 1977, *Raes* 1995]. In addition, the remote marine FT also includes air masses transported long distances from continents which likely contain some pollution aerosol.

We derive a value of N_{FT} in the range 100-175 cm^{-3} active at σ=0.3% from the mean Mauna Loa size distribution (assuming a plausible range of aerosol hygroscopicity, see caption, Fig. 1). This is in remarkable agreement with mean values from CCN

spectrum measurements made in the southern hemisphere subtropical FT during VOCALS-REx (see Fig. 2a). For the model base case we therefore assume a constant mean concentration $N_{FT} = 125$ cm^{-3} everywhere, which is within 20% of the time-mean values derived from the remote subtropical data in both hemispheres. We also force the model with observed values of FT CCN from VOCALS-REx and conduct additional sensitivity tests, as described in Section 4.

3.3 Sea surface source

For the surface source, we use a size-resolved sea spray generation function [*Clarke et al.* 2006] to estimate the rate of particle generation for particles active at σ=0.3% supersaturation. This yields $F(\sigma) = 214$ m^{-3} (m s^{-1})$^{-2.41}$. For a wind speed of 8 m s^{-1} this yields $\dot{N}_S = 22$ cm^{-3} d^{-1} averaged over an MBL that is 1 km deep. The widely-used source function of *Monahan et al.* [1986] has the same wind speed dependence but a rate which is over a factor of two lower.

To drive SSA production we use daily mean wind speed estimates from the QuikScat satellite and average the production rates up to monthly averages. Including sub-daily timescale variability in wind speed increases the surface production of SSA, but we find from reanalysis data that including 6 hourly estimates increases SSA production by less than 10%.

3.4 Precipitation sink

The model sink term is driven by new precipitation rate estimates from the profiling W-band radar on the CloudSat satellite [*Lebsock and L'Ecuyer* 2011]. The

cloud base precipitation rate needed to calculate the coalescence scavenging [*Wood* 2006] is estimated as the maximum value in each radar profile. Mean precipitation rates from low clouds are estimated for 5×5° gridboxes globally by removing profiles with detectable echoes above the 3 km level. For the regions considered, the results are not strongly sensitive to the choice of this level since the majority of the clouds are situated below 2 km. Gridded precipitation rates are produced on a monthly basis for data from 2006-2009.

We also use precipitation measurements from VOCALS-REx to compare against those from CloudSat. For this, we use both aircraft in-situ observations from an optical array probe, and aircraft radar measurements from the University of Wyoming Cloud Radar. The VOCALS-REx precipitation dataset is described in *Bretherton et al.* [2010]. The majority of the aircraft flights were conducted during the later part of the night (03-09 local time) when precipitation rates are at their diurnal maximum.

3.5 Boundary layer depth, cloud thickness, wind speed, and surface divergence.

Equation (2) indicates that we also need to estimate MBL depth z_i, cloud thickness h, surface wind speed U_{10}, and surface divergence D. MBL depth is estimated using from MODIS cloud top temperature retrievals [*Wood and Bretherton* 2004]. Cloud thickness h is estimated with an adiabatic assumption using MODIS retrievals of cloud liquid water path. Both are taken from 1×1° gridded daily Level 3 MODIS products. The results are not strongly sensitive to these parameters. Wind speed and surface divergence estimates are from the QuikScat satellite [see *Wood et al*. 2009 for details].

296 3.5. Cloud droplet concentration

297 Satellite estimates of cloud droplet concentration are used to compare against
298 model-derived N_{eq} from Equation (2). Model estimates are produced globally on a 1×1°
299 grid on a month by month basis. Cloud droplet concentration estimates from the
300 Moderate Resolution Imaging Spectroradiometer (MODIS) on the NASA Terra satellite
301 are produced from daily Level 3 data for 1x1° boxes using a visible/near infrared
302 approach [*Bennartz* 2007]. To minimize problems of retrievals in broken clouds, we only
303 include in our averages those daily boxes where the cloud cover from liquid clouds
304 exceeds 0.8. These are then averaged together to provide monthly mean N_d estimates.
305

306 3.6. Model estimates of N_d

307 We use the budget model Equation (2) to predict monthly mean values of N_d by
308 forcing with monthly-mean values of the input variables discussed above. Annual means
309 are then derived from the monthly means only for those months with (a) mean subsidence
310 (positive mean surface divergence); (b) mean boundary layer depth lower than 4 km; and
311 (c) with mean liquid cloud fractions exceeding 0.3. Annual mean data are only analyzed
312 for those locations where at least four months pass the acceptance criteria.
313

314 **4. Results**

315 4.1 Model assessment over the southeastern Pacific

316 To assess the quality of the model, we use recent field measurements from VOCALS-
317 REx that extensively sampled the lower troposphere over the tropical southeastern Pacific

318 Ocean [*Wood et al.* 2011]. The measurements focused upon characterizing the largest
319 semi-permanent subtropical sheet of stratocumulus on Earth that extends westward from
320 the Chilean and Peruvian coasts. Extensive survey sampling was carried out along 20°S
321 from the Chilean coast at 70°W to ~1400 km offshore at 85°W using a combination of
322 different research aircraft. Measurements were made in both the MBL and the lower FT.
323 Figure 2a shows observations of the two key inputs to the budget model, namely the
324 time-mean FT CCN concentration (section 3.2) and the precipitation rate close to the
325 cloud base (section 3.4). CCN concentrations in the FT fall off sharply within 500 km of
326 the coast but despite considerable day to day variability, the time-mean campaign values
327 remain relatively constant for over 1000 km out to 85°W (Fig 2a). Several lines of
328 evidence point to anthropogenic pollution being responsible for the high values very
329 close to the coast [*Allen et al.* 2011, *Yang et al.* 2011, *Saide et al.* 2012].
330 The cloud base precipitation rate increases markedly with distance from the
331 Chilean coast, from an essentially nonprecipitating state with <0.1 mm d^{-1} near the coast
332 to >1 mm d^{-1} at 85°W (Fig. 2a). Rates of a few tenths of a mm d^{-1} are sufficient to drive
333 significant coalescence scavenging of CCN [*Feingold et al.* 1996, *Wood* 2006]. This
334 gradient in precipitation is driven to a significant extent by thickening clouds and a
335 deeper boundary layer to the west [*Bretherton et al.* 2010], but is likely also modulated
336 by aerosol in the MBL [*Terai et al.* 2012]. The cause of the precipitation is not the focus
337 of this study. Precipitation production in marine stratocumulus maximizes at night [*Leon*
338 *et al.* 2008], and is typically heaviest in the early morning hours when the clouds are at
339 their thickest [*Bretherton et al.* 2004, *Wood et al.,* 2002]. This is apparent in the
340 observations where precipitation rates are lowest at 1:30pm (CloudSat, daytime overpass,

341 Fig. 2a), take intermediate values at 1:30am (CloudSat nighttime overpasss) and are
342 largest during 03-09 am (VOCALS field data). Since the timescale for CCN removal due
343 to precipitation is typically at least 1 day given these precipitation rates [*Wood* 2006], we
344 use a daily mean estimate as the mean of the two CloudSat overpasses to drive the model.
345 The model, when forced with CloudSat observed mean precipitation rates and
346 observed FT CCN, captures the observed increase in N_d as the coast is approached (Fig.
347 2b) with remarkable fidelity given the model's simplicity. The model predicts a factor of
348 two increase in N_d from 90°W to 75°W even when the model is forced with a fixed FT
349 CCN concentration of 125 cm^{-3} (consistent with mean values over the remote region
350 away from the coast). With fixed CCN, however, the model is unable to reproduce the
351 highest concentrations within 500 km of the coast (Fig. 2b). However, these high values
352 are obtained when the model is forced with the observed longitudinally-varying FT CCN
353 concentration increase that includes the near-coastal enhancement due to pollution
354 sources [*Allen et al.* 2011] (Fig 2b). The general behavior of decreasing N_d westward
355 from 75-90°W is caused by increasing precipitation scavenging (Fig. 2a), which can be
356 seen by comparing the model estimates with fixed FT CCN and either no precipitation or
357 precipitation fixed at a constant value of 1 mm d^{-1} (Fig 2b). A critical finding here is that
358 a precipitation rate of as little as 1 mm d^{-1} is sufficient to drive down N_d by a factor of
359 three over the remote ocean, which further serves to emphasize how important
360 precipitation from low clouds is in controlling mean cloud droplet concentrations over the
361 remote ocean.
362 Primary production from sea-spray constitutes a weaker, but nevertheless
363 significant, source than entrainment from the FT consistent with a previous study with the

same parameterization [*Clarke et al.* 2006]. However, it is important to note that we are using a source function that is one of the more prolific available [*de Leeuw et al*. 2011], although experimentation with different primary production parameterizations only changes the modeled N_d values by less than 20% (Fig. 3). The CCN concentration from sea-salt (the difference between the solid and the dotted line in Fig. 3) ranges from <10 cm^{-3} close to the Chilean coast, where wind speeds are low, to around 40 cm^{-3} further afield, where wind speeds are higher. These findings are consistent with preliminary measurements of sea-salt particles from aircraft during VOCALS-REx (Anthony Clarke, personal communication). The choice of sea-spray parameterization does not affect our conclusions regarding the importance of precipitation at driving the offshore gradient in cloud droplet concentration over the southeastern Pacific.

4.2 Application to marine low cloud regions globally

Given the ability of the budget model with fixed FT CCN concentrations to reproduce with some skill the gradient in N_d over the remote southeastern Pacific Ocean (more than 500 km from the coast), we apply the model more generally to regions of extensive marine low cloud under conditions of large scale subsidence (Fig. 4). Aerosol concentrations in the FT vary significantly both regionally and in response to variations in natural and anthropogenic sources [*Allen et al.* 2011]. Because there are no global observational constraints on the time-mean FT CCN, we draw on the consistency between mean FT CCN spectra at Mauna Loa and over the southeastern Pacific Ocean (Fig. 1 and section 3.2) and fix N_{FT} = 125 cm^{-3} everywhere for the base case. The satellite observations show that N_d values in excess of 150 cm^{-3} tend to be located near the

387 continental coastlines (e.g. California, Chile/Peru, Europe), with values reducing toward
388 the remote oceans, where they are as low as 30-60 cm^{-3} (Fig. 4a). The base case model is
389 able to reproduce well the mean values (Table 1) and geographical variability in N_d (Fig.
390 4) for low cloud regions, especially for the remote subtropical/tropical regions 35°S-
391 35°N. The model underestimates N_d close to coastlines (Table 1) consistent with a lack of
392 continental sources. The model also captures the low values (<60 cm^{-3}) over the remote
393 North Pacific and Atlantic and the Southern Ocean north of 45°S. Removing the
394 precipitation sink increases mean N_d in the model by a factor of 2-3 over the remote
395 oceans, but only 15% in the near-coastal regions where precipitation rates are very low
396 (Table 1). A doubling of N_{FT} from 80 to 160 cm^{-3} leads to a 50-70% increase in N_d
397 (Table 1) because FT CCN is partly buffered by surface sources.
398 The skill of the base case model in predicting N_d variability is remarkable given
399 that there is no variation whatsoever in the FT CCN source in Fig. 4. To examine the key
400 factors controlling the geographical variability of N_d in the model, we conduct additional
401 model sensitivity experiments. In each experiment, only one (or two) of the variables in
402 equation (2) is allowed to vary. All other variables are fixed by setting them to their
403 respective mean values over time and space (Table 2). It is clear that precipitation
404 variability is required in order to produce the strong correlation with observations seen in
405 the base case (r = 0.65). No other variable can alone explain more than 15% of the
406 observed geographical variance in N_d. Divergence and cloud thickness variations also
407 lead to model fields with significant positive correlations (r =0.21 and 0.37 respectively),
408 but the geographical variability in N_d driven by these variables is far too weak to explain
409 the observed variability (Table 2). The correlations are positive because divergence and

410 cloud thickness correlate quite well with precipitation itself. We find that wind speed
411 variability alone explains an insignificant amount of the model N_d variability (r = -0.06),
412 from which we conclude that variability in SSA is not a significant contributor to the
413 observed geographical variability in N_d. This is especially true in the subtropics and
414 tropics where wind speeds are relatively modest and the FT source is greater than the
415 surface source (Fig. 5). However, SSA does contribute to the mean N_d (Table 1) despite
416 not substantially impacting its geographical variability.

417 Overall, these results lead us to argue that a large fraction of the observed
418 geographical variability in cloud droplet concentration in extensive marine low clouds
419 over the remote oceans is driven by precipitation losses rather than aerosol source
420 variability. This is further demonstrated by noting the striking similarities between the
421 maps of the mean observed precipitation rates from low clouds (Fig. 6) and the observed
422 N_d field (Fig. 4a).

423 Frequency distributions of monthly mean N_d (Fig. 7) show that the base case
424 model (N_{FT} = 125 cm^{-3}) can represent satellite-observed N_d variability well. As we might
425 expect from Fig. 2, the model is unable to capture the very highest concentrations
426 observed by the satellite (N_d > 200 cm^{-3}) that are mostly regions within a few hundred
427 kilometers of coastlines. This is because neither the advection of continentally-influenced
428 MBL air nor elevated near-coastal FT concentrations (e.g., Fig. 2) are considered in the
429 model. When the model is forced by removing either FT CCN or SSA production, the
430 model is unable to represent the distribution of observed N_d and underestimates the mean
431 N_d (Fig. 7 and see also Table 1). This further emphasizes that the surface and FT are both
432 important contributors to the cloud droplet concentration over the remote oceans

433 [*Katoshevski et al.* 1999, *Capaldo et al.* 1999, *Clarke et al.* 2006]. The shape of the
434 model N_d distribution is relatively insensitive to plausible variations in the assumed mean
435 FT CCN concentration (Fig. 8).
436
437 **5. Implications and conclusions**

438 Our results have a number of important implications. First, if CCN and cloud
439 droplet concentration variability over much of the global ocean are determined by
440 precipitation variability rather than aerosol source variability, this calls into question the
441 interpretation of correlative studies [*Quaas et al.* 2008, *Jones et al.* 2009] linking cloud
442 properties to aerosol properties as providing useful information on anthropogenic aerosol
443 indirect effects on climate. It also suggests that the notion of there being a 'background'
444 aerosol concentration in the unperturbed marine boundary layer may not be a useful one
445 because MBL CCN concentrations are strongly modulated by precipitation processes that
446 vary strongly both geographically and temporally. The FT CCN over remote oceanic
447 regions is known to reflect a complex mixture of different sources, some of which are
448 natural and some anthropogenic [*Clarke and Kapustin 2010*]. Our finding that a constant
449 time-mean FT CCN supply is sufficient to explain a significant fraction of the time-mean
450 gradients in the cloud droplet concentration over the remote oceans should not therefore
451 be interpreted as indicating that the remote oceanic regions are devoid of anthropogenic
452 influence. The increasing concentrations observed within about 500 km of continents
453 most likely reflects a lower tropospheric pathway for the transport of continental aerosols
454 to the MBL, whereas the more remote anthropogenic contributions are associated with

aerosol or precursors lofted higher into the troposphere that can then be transported long distances before subsidence carries them into the MBL.

Here we have shown that MBL cloud droplet concentrations are impacted by precipitation generated by the clouds themselves, but we note that an increasing body of evidence shows that precipitation in low clouds typically decreases with cloud droplet concentration [*Stevens and Feingold* 2009]. There is then the potential for a significant positive feedback whereby modest increases in CCN reduce the precipitation sink, amplifying the initial perturbation. Although we do not claim evidence for bistability in the system [*Baker and Charlson* 1990], our results do suggest that pollution-driven CCN increases may be amplified by precipitation suppression and that this warrants further exploration with more sophisticated models. There is modeling evidence for this in the recent literature [*Yang et al.* 2012].

Finally, we note that climate models tend to impose arbitrary fixed limits on cloud droplet concentration minima [*Quaas et al.* 2009] suggesting deficiencies in modeling the processes responsible for low concentrations over the remote ocean. Across models, there is a significant correlation between this fixed lower limit on N_d and the strength of the aerosol indirect effect [*Quaas et al.* 2009]. A closer focus on the role of precipitation is therefore needed to better understand whether climate models are able to produce light precipitation in the marine boundary layer, and whether the models are impacted appropriately by it. This study helps to highlight that we now have the satellite measurements of light precipitation and cloud microphysical properties to begin to explore this critical control on cloud microphysical properties.

Acknowledgements:

The authors would like to thank the staff and crew of the NSF/NCAR C-130 aircraft whose dedication resulted in the in-situ observational VOCALS Regional Experiment dataset. The CloudSat data were distributed by the CloudSat Data Processing Center at Colorado State University. MODIS data were obtained from the NASA Goddard Land Processes data archive. QuikScat data were produced by Remote Sensing Systems and sponsored by the NASA Ocean Vector Winds Science Team. This work was supported by NASA award numbers NNX10AN78G and NNX10AM29G and NSF award numbers ATM-0745702 and ATM-0745368.

References

Allen, G., Coe, H., Clarke, A., Bretherton, C., Wood, R., Abel, S. J., Barrett, P., Brown, P., George, R., Freitag, S., McNaughton, C., Howell, S., Shank, L., Kapustin, V., Brekhovskikh, V., Kleinman, L., Lee, Y.-N., Springston, S., Toniazzo, T., Krejci, R., Fochesatto, J., Shaw, G., Krecl, P., Brooks, B., McMeeking, G., Bower, K. N., Williams, P. I., Crosier, J., Crawford, I., Connolly, P., Allan, J. D., Covert, D., Bandy, A. R., Russell, L. M., Trembath, J., Bart, M., McQuaid, J. B., Wang, J., and Chand, D.: South East Pacific atmospheric composition and variability sampled along 20° S during VOCALS-REx, Atmos. Chem. Phys., 11, 5237-5262, doi:10.5194/acp-11-5237-2011 (2011).

Baker, M. B., and R. L. Charlson. Bistability of CCN concentrations and thermodynamics in the cloud-topped boundary layer. *Nature,* **345,** 142–145 (1990).

Baker, M. B. Variability in concentrations of cloud condensation nuclei in the marine cloud-topped boundary layer. *Tellus,* **45B,** 458–472 (1993).

509 Bennartz, R. Global assessment of marine boundary layer cloud droplet number
510 concentration from satellite, J. Geophys. Res., 112, D02201 (2007).

511 Bennartz, R., J. Fan, J. Rausch, L. R. Leung, and A. K. Heidinger. Pollution from China
512 increases cloud droplet number, suppresses rain over the East China Sea, Geophys.
513 Res. Lett., 38, L09704, doi:10.1029/2011GL047235 (2011).

514 Bréon, F. M., Tanre, D., Generoso, S. Aerosol effect on cloud droplet size monitored
515 from satellite. *Science*, **295,** 834-838 (2002).

516 Bretherton, C. S., Wood, R., George, R. C., Leon, D., Allen, G., and Zheng, X.: Southeast
517 Pacific stratocumulus clouds, precipitation and boundary layer structure sampled
518 along 20°S during VOCALS-REx, *Atmos. Chem. Phys*., **10**, 10639-10654 (2010).

519 Capaldo K. P., Kasibhatla P., and Pandis S.N. Is aerosol production within the remote
520 marine boundary layer sufficient to maintain observed concentrations? *J. Geophys.*
521 *Res.,***104**, 3483-3500 (1999).

522 Clarke, A. D., et al., Particle nucleation in the tropical boundary layer and its coupling to
523 marine sulfur sources, Science, 282, 89– 92 (1998a).

524 Clarke, A. D., J. L. Varner, F. Eisele, R. L. Mauldin, D. Tanner, and M. Litchy. Particle
525 production in the remote marine atmosphere: Cloud outflow and subsidence during
526 ACE 1, *J. Geophys. Res.*, 103(D13), 16,397–16,409 (1998b).

527 Clarke, A. D., S. R. Owens, and J. Zhou. An ultrafine sea-salt flux from breaking waves:
528 Implications for cloud condensation nuclei in the remote marine atmosphere, *J.*
529 *Geophys. Res*., **111**, D06202 (2006).

530 Clarke, A. D., and Kapustin, V.: Hemispheric aerosol vertical profiles: anthropogenic
531 impacts on optical depth and cloud nuclei, *Science*, **329**, 1488–1492, (2010)

532 de Leeuw, G., E. L Andreas, M. D. Anguelova, C. W. Fairall, E. R. Lewis, C. O'Dowd,
533 M. Schulz, and S. E. Schwartz: Production flux of sea spray aerosol, *Rev. Geophys*.,
534 **49**, RG2001 (2011).

535 Feingold, G., S. M. Kreidenweis, B. Stevens, and W. R. Cotton. Numerical simulations of
536 stratocumulus processing of cloud condensation nuclei through collision-coalescence,
537 J. Geophys. Res., 101, 21,391–21,402 (1996).

538 Friedlander, S.K. *Smoke, dust and haze*. John Wiley and Sons (1977).

539 George, R. C. and Wood, R. Subseasonal variability of low cloud radiative properties
540 over the southeast Pacific Ocean, *Atmos. Chem. Phys*., **10**, 4047-4063,
541 doi:10.5194/acp-10-4047-2010 (2010).

542 Gettelman, A., H. Morrison, S. J. Ghan. A New Two-Moment Bulk Stratiform Cloud
543 Microphysics Scheme in the Community Atmosphere Model, Version 3 (CAM3).
544 Part II: Single-Column and Global Results. *J. Climate*, **21**, 3660–3679 (2008).

545 Giorgi, F. Dry deposition velocities of atmospheric aerosols as inferred by applying a
546 particle dry deposition parameterization to a general circulation model. *Tellus B*, **40B**,
547 23-41 (1988).

548

549 Haynes, J. M., T. S. L'Ecuyer, G. L. Stephens, S. D. Miller, C. Mitrescu, N. B. Wood,
550 and S. Tanelli. Rainfall retrieval over the ocean with spaceborne W-band radar, J.
551 Geophys. Res., 114, D00A22, (2009).

552 Hoppel, W. A., Frick, G. M., and Larson, R. E.: Effects of nonprecipitating clouds on the
553 aerosol size distribution in the marine boundary layer, Geophys. Res. Lett., 13, 125–
554 128, 1986.

555 IPCC, 2007. Climate Change: The Physical Science Basis. Contribution of Working
556 Group I to the Fourth Assessment Report of the Intergovernmental Panel on Climate
557 Change. S. Solomon, D. Qin, M. Manning, Z. Chen, M. Marquis, K.B. Averyt,
558 M.Tignor and H.L. Miller (eds.) Cambridge University Press, Cambridge, United
559 Kingdom and New York, NY, USA (2007).

560 Isaksen, I. S. A. et al. Atmospheric composition change: Climate–Chemistry interactions.
561 *Atmospheric Environment*, **43**, 5138-5192 (2009).

562 Jones, T. A., Christopher, S. A., and Quaas, J. A six year satellite-based assessment of the
563 regional variations in aerosol indirect effects, *Atmos. Chem. Phys.*, **9**, 4091-4114,
564 (2009).

565 Katoshevski, D., Nenes, A., and Seinfeld, J. H. A Study of processes that govern the
566 maintenance of aerosols in the marine boundary layer, *J. Aerosol Sci.*, **30**, 503-532
567 (1999).

568 Kaufman, Y., D. Tanré, and O. Boucher. A satellite view of aerosols in the climate
569 system. *Nature*, **419**, 215-223 (2002).

570 Kirkby, J., et al., Role of sulphuric acid, ammonia and galactic cosmic rays in
571 atmospheric aerosol nucleation. *Nature*, **476**, 429-433 (2011).

572 Klein, S. A. and D. L. Hartmann. The seasonal cycle of low stratiform clouds. *J.*
573 *Climate*,, 6, 1588–1606 (1993).

574 Kleinman, L. I., Daum, P. H., Lee, Y.-N., Lewis, E. R., Sedlacek III, A. J., Senum, G. I.,
575 Springston, S. R., Wang, J., Hubbe, J., Jayne, J., Min, Q., Yum, S. S., and Allen, G.:
576 Aerosol concentration and size distribution measured below, in, and above cloud
577 from the DOE G-1 during VOCALS-REx, Atmos. Chem. Phys., 12, 207-223,
578 doi:10.5194/acp-12-207-2012, 2012.

579 Lebsock, M. D., and T. S. L'Ecuyer, The retrieval of warm rain from CloudSat, *J.*
580 *Geophys. Res.*, doi:10.1029/2011JD016076 (2011).

581 Leon, D. C., Z. Wang, and D. Liu. Climatology of drizzle in marine boundary layer
582 clouds based on 1 year of data from CloudSat and Cloud-Aerosol Lidar and Infrared
583 Pathfinder Satellite Observations (CALIPSO), J. Geophys. Res., 113, D00A14
584 (2008).

585 Lohmann, U., and J. Feichter. Global indirect aerosol effects: a review. *Atmos. Chem.*
586 *Phys. Disc.* 5, 715–737 (2005).

587 Martin, G. M., D. W. Johnson, and A. Spice. The measurement and parameterization of
588 effective radius of droplets in warm stratocumulus clouds. *J. Atmos. Sci.*, 51, 1823–
589 1842 (2004).

590 Ming, Y, V. Ramaswamy, L. J Donner, and V. T. J. Phillips. A new parameterization of
591 cloud droplet activation applicable to general circulation models**.** *J. Atmos. Sci.*., **63**,
592 DOI:10.1175/JAS3686.1 (2006).

593 Monahan, E. C., D. E. Spiel, and K. L. Davidson (1986), A model of marine aerosol
594 generation via whitecaps and wave disruption, in Oceanic Whitecaps and Their Role
595 in Air-Sea Exchange Processes, edited by E. C. Monahan and G. Mac Niocaill, pp.
596 167– 193, Springer, New York.

597 Oreopoulos L., and S. Platnick. The radiative susceptibility of cloudy atmospheres to
598 droplet number perturbations: 2. Global analysis from MODIS *J. Geophys. Res.,* **113***,*
599 D14S21 (2008).

600 Penner, J. E., X. Q. Dong, and Y. Chen. Observational evidence of a change in radiative
601 forcing due to the indirect aerosol effect. *Nature*., **427**, 231-234 (2004).

602 Petters, M. D. and Kreidenweis, S. M.: A single parameter representation of hygroscopic
603 growth and cloud condensation nucleus activity, Atmos. Chem. Phys., 7, 1961-1971,
604 doi:10.5194/acp-7-1961-2007, 2007.

605 Platnick, S., and S. Twomey, 1994: Determining the susceptibility of cloud albedo to\
606 changes in droplet concentrations with the advanced very high resolution radiometer.
607 *J. Appl. Meteorol*., **33**, 334-347.

608 Quaas, J., O. Boucher, N. Bellouin, and S. Kinne. Satellite-based estimate of the direct
609 and indirect aerosol climate forcing, *J. Geophys. Res.*, 113, D05204,
610 doi:10.1029/2007JD008962 (2008).

611 Quaas, J et al. Aerosol indirect effects – general circulation model intercomparison and
612 evaluation with satellite data, *Atmos. Chem. Phys*., **9**, 8697-8717 (2009).

613 Ramanathan, V., P. J. Crutzen, J. T. Kiehl, and D. Rosenfeld. Aerosols, climate, and the
614 hydrological cycle. *Science*. **294**, 2119-2124 (2001).

615 Roberts, G. C., Day, D. A., Russell, L. M., Dunlea, E. J., Jimenez, J. L.,
616 Tomlinson, J. M., Collins, D. R., Shinozuka, Y., and Clarke, A. D.: Characterization
617 of particle cloud droplet activity and composition in the free troposphere and the

618 boundary layer during INTEX-B, Atmos. Chem. Phys., 10, 6627-6644,
619 doi:10.5194/acp-10-6627-2010, 2010.

620 Saide, P. E., Spak, S. N., Carmichael, G. R., Mena-Carrasco, M. A., Yang, Q., Howell,
621 S., Leon, D. C., Snider, J. R., Bandy, A. R., Collett, J. L., Benedict, K. B., de Szoeke,
622 S. P., Hawkins, L. N., Allen, G., Crawford, I., Crosier, J., and Springston, S. R.:
623 Evaluating WRF-Chem aerosol indirect effects in Southeast Pacific marine
624 stratocumulus during VOCALS-REx, Atmos. Chem. Phys., 12, 3045-3064,
625 doi:10.5194/acp-12-3045-2012, 2012

626 Snider, J. R., M. D. Petters, P. Wechsler and P. Liu, Supersaturation in the Wyoming
627 CCN instrument, *J. Atmos. Oceanic Technol.*, 23, 1323-1339, 2006.

628 Twomey, S., 1974: Pollution and the planetary albedo. *Atmos. Env.*, 8, 1251–1256.

629 Petters, M. D., J. R. Snider, B. Stevens, G. Vali, I. Faloona, and L. M. Russell (2006),
630 Accumulation mode aerosol, pockets of open cells, and particle nucleation in the
631 remote subtropical Pacific marine boundary layer, J. Geophys. Res., 111, D02206,
632 doi:10.1029/2004JD005694.

633 Raes, F. Entrainment of free tropospheric aerosols as a regulating mechanism for cloud
634 condensation nuclei in the remote marine boundary layer, *J. Geophys. Res.*, **100**,
635 2893–2903 (1995).

636 Snider, J. R., S. Guibert, J. L. Brenguier, and J. P. Putaud. Aerosol activation in marine
637 stratocumulus clouds: 2. Kohler and parcel theory closure studies. *J. Geophys. Res.,*
638 **108**, 8629 (2003).

639 Stevens, B. Entrainment in stratocumulus-topped mixed layers. *Quarterly Journal of the*
640 *Royal Meteorological Society* **128**, 2663–2690 (2002).

641 Stevens, B., and G. Feingold. Untangling aerosol effects on clouds and precipitation in a
642 buffered system. *Nature*, **461**, doi:10.1038/nature08281 (2009).

643 Terai, C. R., Wood, R., Leon, D. C., and Zuidema, P.: Does precipitation susceptibility
644 vary with increasing cloud thickness in marine stratocumulus?, *Atmos. Chem. Phys.*,
645 12, 4567-4583, doi:10.5194/acp-12-4567-2012, 2012.

646 Tomlinson, J. M., R. Li, and D. R. Collins. Physical and chemical properties of the
647 aerosol within the southeastern Pacific marine boundary layer, J. Geophys. Res., 112,
648 D12211 (2007).

649 Weber, R. J. and P. H. McMurry. Fine particle size distribution measurements at Mauna
650 Loa Observatory, Hawaii, *J. Geophys. Res*., **101**, 14767-14775 (1996).

651 Wood, R., C. S. Bretherton, and D. L. Hartmann. Diurnal cycle of liquid water path over
652 the subtropical and tropical oceans. *Geophys. Res. Lett.* **10**.1029/2002GL015371
653 (2002).

654 Wood, R., and C.S. Bretherton. Boundary layer depth, entrainment and decoupling in the
655 cloud-capped subtropical and tropical marine boundary layer. *J. Clim.* 17, 3576–3588
656 (2004).

657 Wood, R., The rate of loss of cloud droplets by coalescence in warm clouds. *J.Geophys.*
658 *Res*., **111**, D21205 (2006).

659 Wood, R., K. K. Comstock, C. S. Bretherton, C. Cornish, J. Tomlinson, D. R. Collins,
660 and C. Fairall. Open cellular structure in marine stratocumulus sheets, *J. Geophys.*
661 *Res.*, 113, D12207 (2008).

662 Wood, R., M. Köhler, R. Bennartz, C. O'Dell. The diurnal cycle of surface divergence
663 over the global oceans. *Quart. J. Roy. Meteorol. Soc*., **135,** 1484-1493 (2009).

664 Wood, R. et al. The VAMOS Ocean-Cloud-Atmosphere-Land Study Regional
665 Experiment (VOCALS-REx): goals, platforms, and field operations, *Atmos. Chem.*
666 *Phys*., **11**, 627-654 (2011).

667 Yang, Q., W. I. Gustafson Jr., Fast, J. D., Wang, H., Easter, R. C., Morrison, H., Lee, Y.-
668 N., Chapman, E. G., Spak, S. N., and Mena-Carrasco, M. A.: Assessing regional scale
669 predictions of aerosols, marine stratocumulus, and their interactions during
670 VOCALS-REx using WRF-Chem, Atmos. Chem. Phys., 11, 11951-11975,
671 doi:10.5194/acp-11-11951-2011, 2011.

672
673

Figure Captions

Figure 1: Free-tropospheric CCN spectra from the southeastern Pacific and Hawaii. Observations from the southeastern Pacific are from CCN spectra taken in the remote FT west of 75°W using the NSF/NCAR C-130 aircraft in VOCALS-REx [*Wood et al.* 2011], corrected to an assumed mean MBL pressure of 925 hPa. Box-whisker plots show the 10^{th}, 25^{th}, 50^{th} , 75^{th}, and 90^{th} percentile concentrations for four supersaturations. Shaded region shows a plausible range of CCN concentration estimated using the composite size distribution for subsiding FT air measured on Mauna Loa in Hawaii [*Weber and McMurry* 1996], corrected to an assumed mean MBL pressure of 925 hPa, with the spread representing a plausible range of hygroscopicity κ parameters [*Petters and Kreidenweis* 2007] for clean FT air (see text).

Figure 2: Model inputs and results from southeastern Pacific stratocumulus region from 70-90°W along 20°S. (a) Free-tropospheric (FT) aerosol concentrations (left axis) showing range of mean CCN concentrations corresponding to supersaturations relevant for cloud formation (gray shading), and total non-volatile particle concentration (open circles). Green bar shows estimated CCN for 0.2-0.5% supersaturation from measurements of FT aerosol size distributions during subsiding conditions on Mauna Loa, Hawaii, see the Methods section; cloud base precipitation rates (right axis) estimated from CloudSat satellite (mean for October/November 2006-2009 between 22°S and 18°S, red shading showing 1:30am and 1:30pm local time overpasses) and from the VOCALS-REx field experiment (black and blue squares from aircraft radar and in-situ precipitation probes respectively, in the latitude range 18-22°S); **(b)** observed (solid circles: aircraft during VOCALS [*Bretherton et al.* 2010, *Wood et al.* 2011], diamonds: satellite estimates from MODIS, 18-22°S) and modeled mean cloud droplet concentration N_d for different model scenarios as denoted in legend and discussed in the text.

Figure 3: Effects of different assumptions regarding primary production of sea-salt in the model. Same as Fig. 2b, but showing sensitivity to sea-salt aerosol parameterization used. Observed (solid circles: aircraft during VOCALS [taken from *Bretherton et al.* 2010], diamonds: satellite estimates from MODIS, 18-22°S) and modeled mean cloud droplet concentration N_d. Solid line: standard model set up with constant FT CCN. Dashed line: Monahan sea-salt parameterization [*Monahan et al.* 1986] in place of *Clarke et al.* [2006]. Dotted line: No primary production of sea-salt at all.

Figure 4: Cloud droplet concentrations in regions of extensive marine low clouds observed by satellite and from the budget model. Annual mean cloud droplet concentration N_d for extensive marine low clouds under conditions of large scale subsidence, (a) from MODIS (see Methods section); (b) from the CCN budget model for the same regions.

Figure 5: Mean precipitation rate at cloud base from low clouds (cloud top height z_{top}<3 km) estimated with spaceborne radar measurements from CloudSat [Lebsock and L'Ecuyer 2011]**.** Data are screened to display regions of extensive marine low clouds under conditions of mean subsidence as in Fig. 4.

Figure 6: Ratio of CCN flux from surface to that from entrainment from the free troposphere (FT) in the model. The FT CCN concentration is set to 125 cm^{-3} and the surface source depends upon daily wind speed. In the subtropics and tropics, the majority of the CCN originate from the FT, but in the midlatitudes where winds are stronger, the surface source can exceed that from the FT.

Figure 7: Frequency distributions of observed and modeled monthly mean cloud droplet concentration. Only months that meet the criteria needed to contribute to the means shown in Fig. 4 (regions with extensive low clouds under divergent conditions) are shown. Shown here are the base version of the model (i.e. that used to construct Fig. 4, solid black), together with estimates with no FT contribution to CCN (dashed), and no sea salt contribution (dotted). Error bars show the 95% confidence interval in the frequency estimates for the observations and for the model base case due to sampling limitations.

Figure 8: Sensitivity to assumed free tropospheric CCN concentration N_{FT} of the frequency distributions modeled monthly mean cloud droplet concentration. Only months that meet the criteria needed to contribute to the means shown in Fig. 4 (regions with extensive low clouds under divergent conditions) are shown. Shown here are the base version of the model (i.e. that used to construct Fig. 4, solid black), together with model estimates with low (N_{FT} = 80 cm^{-3}) and high (N_{FT} = 160 cm^{-3}) estimates of the FT contribution to CCN (dashed blue and orange respectively). Error bars show the 95% confidence interval in the frequency estimates for the observations and for the model base case due to sampling limitations.

TABLES

Table 1: The effects on the mean cloud droplet concentration in various geographical regions of changing the primary source and sink terms

Observed or model estimate	Mean cloud droplet concentration [cm^{-3}]		
	35°S-35°N	35°S-35°N within 300 km of coastlines	60°S-60°N
Observations (MODIS)	**88**	**152**	**74**
Model, base case (N_{FT} = 125 cm^{-3})	88	129	74
Model, N_{FT} = 0	20	21	25
Model, no SSA	68	109	46
Model, no precipitation	169	150	245
Model, N_{FT} = 80 cm^{-3}	63	90	55
Model, N_{FT} = 160 cm^{-3}	107	154	85

Table 2: Geographical variability of cloud droplet concentration for various model configurations. Results show correlation coefficients between annual mean MODIS observed and model estimates of annual mean N_d and the ratio of the model and observed standard deviations ($\sigma_{model}/\sigma_{obs}$). Correlations not significant at the 2σ level are italicized. All results are for the tropics and subtropics (35°S-35°N).

Model configuration	r (obs, model)	$\sigma_{model}/\sigma_{obs}$
Base case	0.65	0.92
P_{CB} variability only	0.77	1.01
P_{CB} and U_{10} variability only	0.70	0.97
U_{10} variability only	*-0.06*	0.37
D variability only	0.21	0.18
h variability only	0.37	0.13
z_i variability only	-0.32	0.10

FIGURES

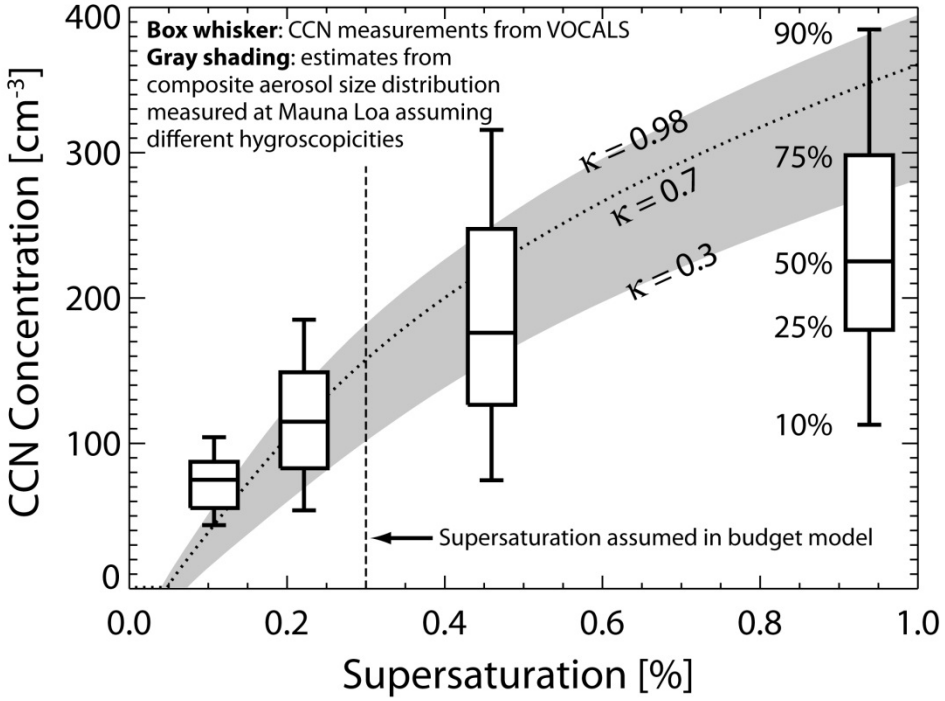

Figure 1: Free-tropospheric CCN spectra from the southeastern Pacific and Hawaii. Observations from the southeastern Pacific are from CCN spectra taken in the remote FT west of 75°W using the NSF/NCAR C-130 aircraft in VOCALS-REx [*Wood et al.* 2011], corrected to an assumed mean MBL pressure of 925 hPa. Box-whisker plots show the 10^{th}, 25^{th}, 50^{th} , 75^{th}, and 90^{th} percentile concentrations for four supersaturations. Shaded region shows a plausible range of CCN concentration estimated using the composite size distribution for subsiding FT air measured on Mauna Loa in Hawaii [*Weber and McMurry* 1996], corrected to an assumed mean MBL pressure of 925 hPa, with the spread representing a plausible range of hygroscopicity κ parameters [*Petters and Kreidenweis* 2007] for clean FT air (see text).

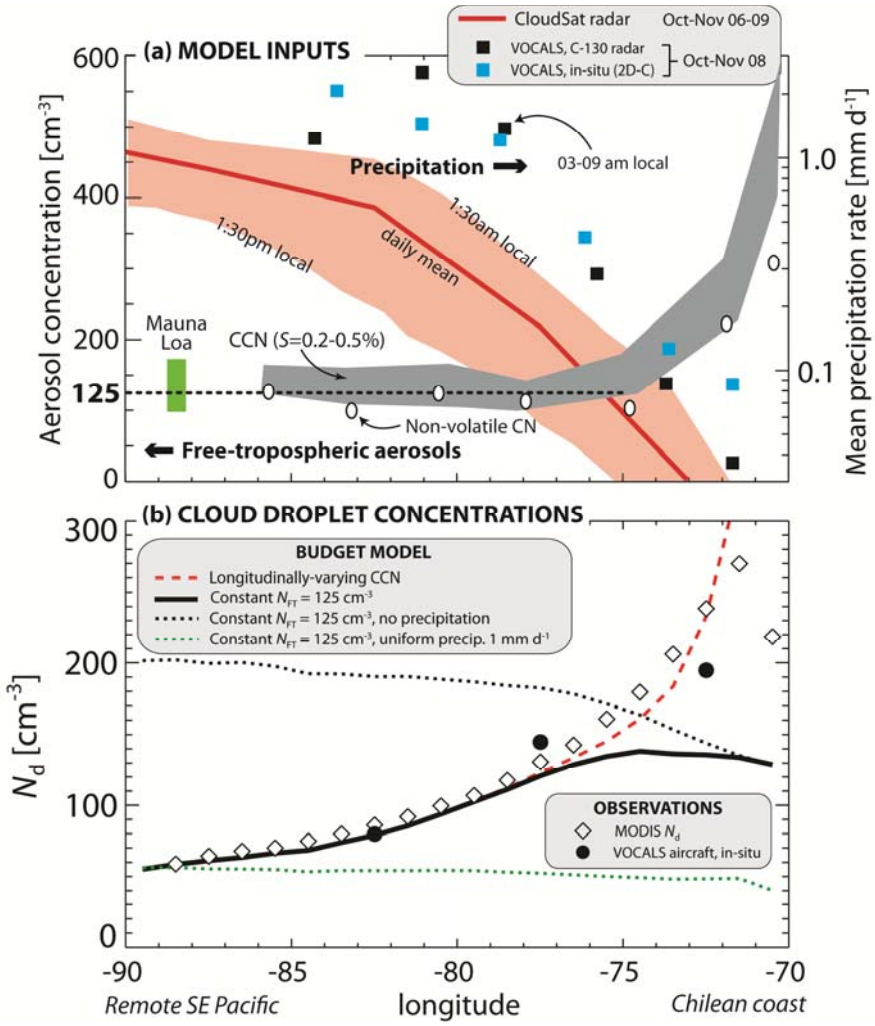

Figure 2: Model inputs and results from southeastern Pacific stratocumulus region from 70-90°W along 20°S. (a) Free-tropospheric (FT) aerosol concentrations (left axis) showing range of mean CCN concentrations corresponding to supersaturations relevant for cloud formation (gray shading), and total non-volatile particle concentration (open circles). Green bar shows estimated CCN for 0.2-0.5% supersaturation from measurements of FT aerosol size distributions during subsiding conditions on Mauna Loa, Hawaii, see the Methods section; cloud base precipitation rates (right axis) estimated from CloudSat satellite (mean for October/November 2006-2009 between 22°S and 18°S, red shading showing 1:30am and 1:30pm local time overpasses) and from the VOCALS-REx field experiment (black and blue squares from aircraft radar and in-situ precipitation probes respectively, in the latitude range 18-22°S); **(b)** observed (solid circles: aircraft during VOCALS [*Bretherton et al.* 2010, *Wood et al.* 2011], diamonds: satellite estimates from MODIS, 18-22°S) and modeled mean cloud droplet concentration N_d for different model scenarios as denoted in legend and discussed in the text.

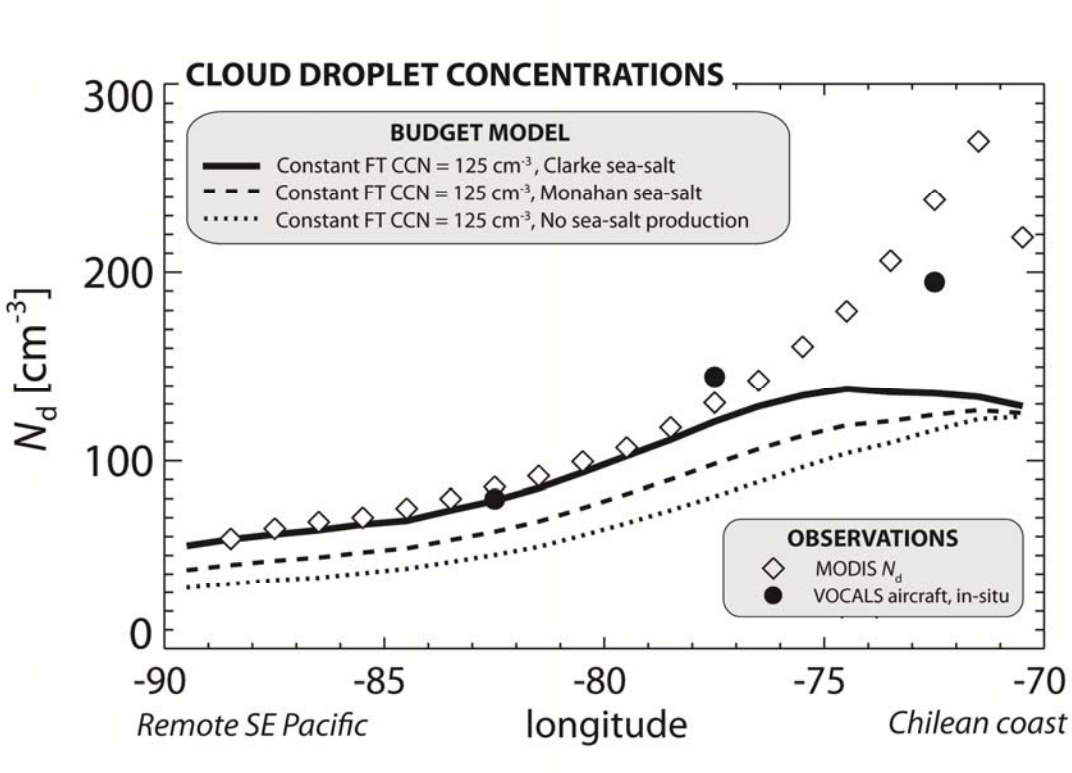

Figure 3: Effects of different assumptions regarding primary production of sea-salt in the model. Same as Fig. 2b, but showing sensitivity to sea-salt aerosol parameterization used. Observed (solid circles: aircraft during VOCALS [taken from *Bretherton et al.* 2010], diamonds: satellite estimates from MODIS, 18-22°S) and modeled mean cloud droplet concentration N_d. Solid line: standard model set up with constant FT CCN. Dashed line: Monahan sea-salt parameterization [*Monahan et al.* 1986] in place of *Clarke et al.* [2006]. Dotted line: No primary production of sea-salt at all.

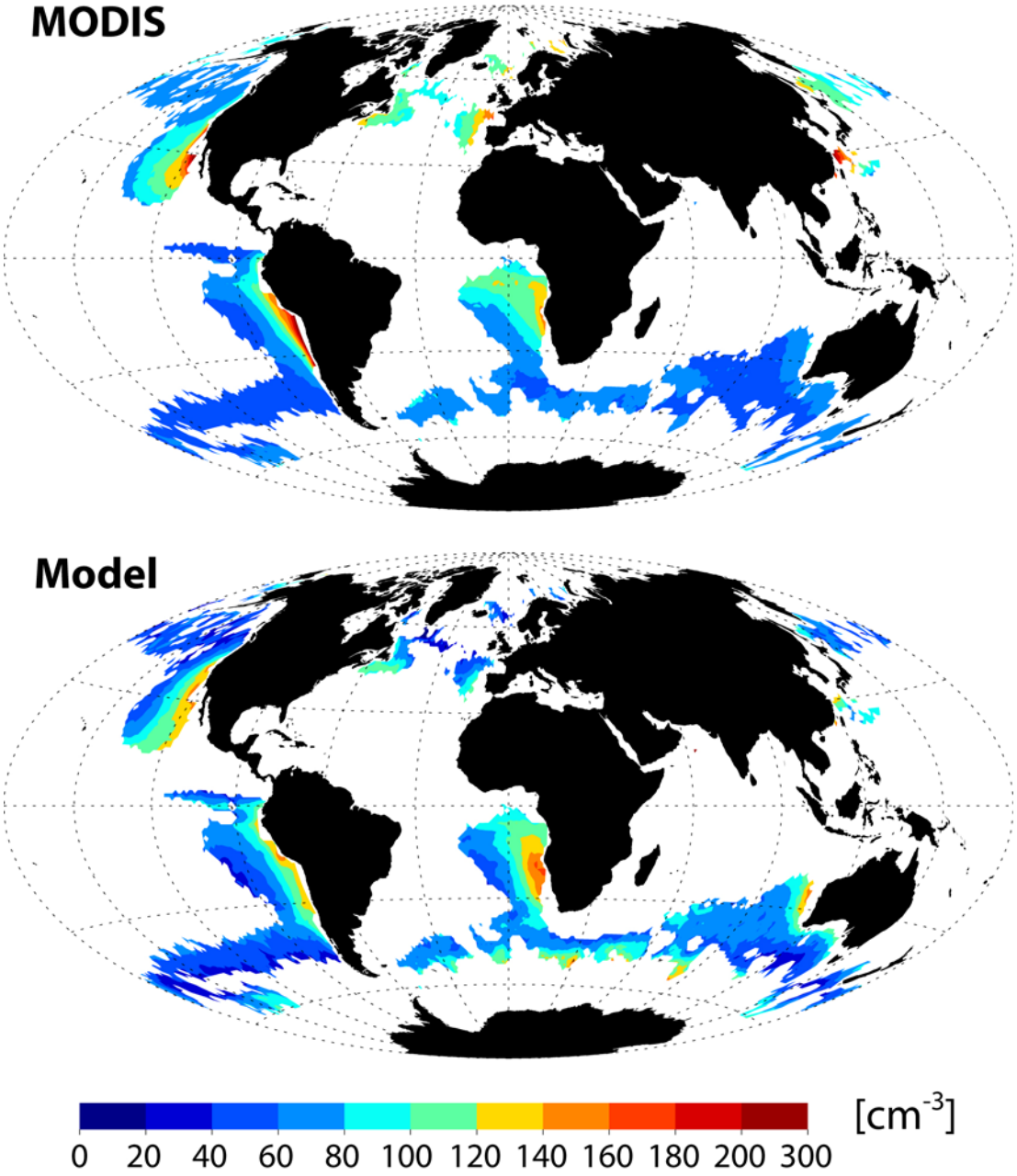

Figure 4: Cloud droplet concentrations in regions of extensive marine low clouds observed by satellite and from the budget model. Annual mean cloud droplet concentration N_d for extensive marine low clouds under conditions of large scale subsidence, (a) from MODIS (see section 3.5); (b) from the steady-state CCN budget model for the same regions.

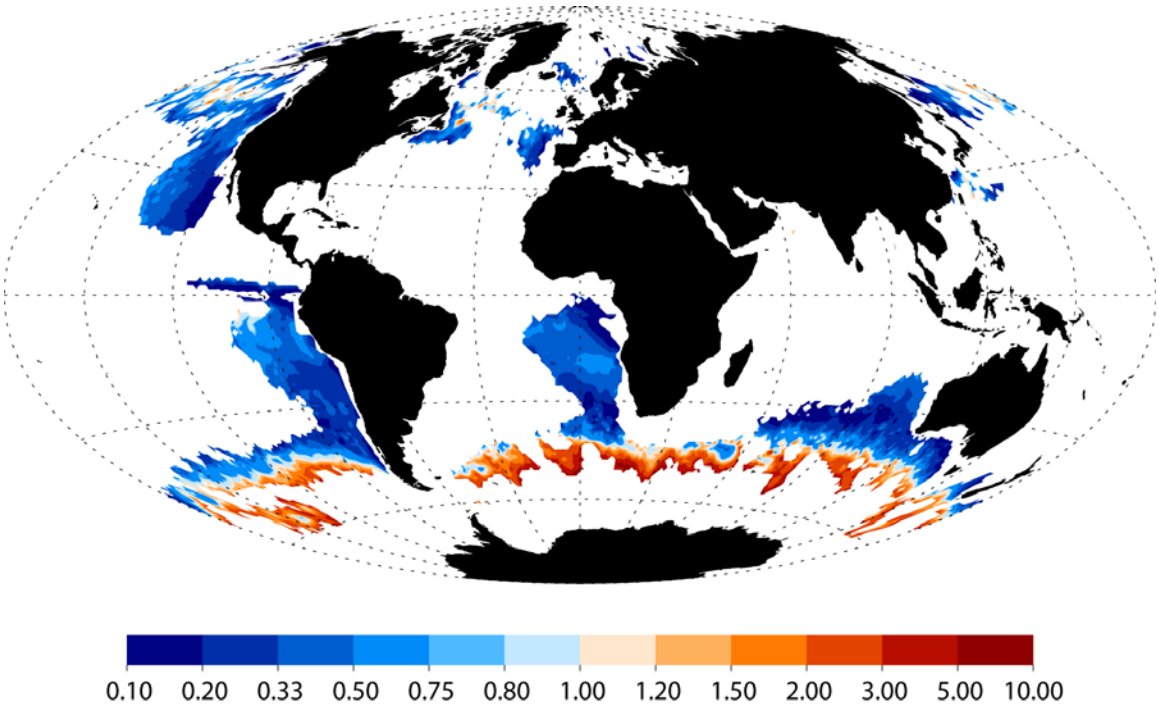

Figure 5: Ratio of CCN flux from surface to that from entrainment from the free troposphere (FT) in the model. The FT CCN concentration is set to 125 cm^{-3} and the surface source depends upon surface wind speed. In the subtropics and tropics, the majority of the CCN originate from the FT, but in the midlatitudes where winds are stronger, the surface source can exceed that from the FT.

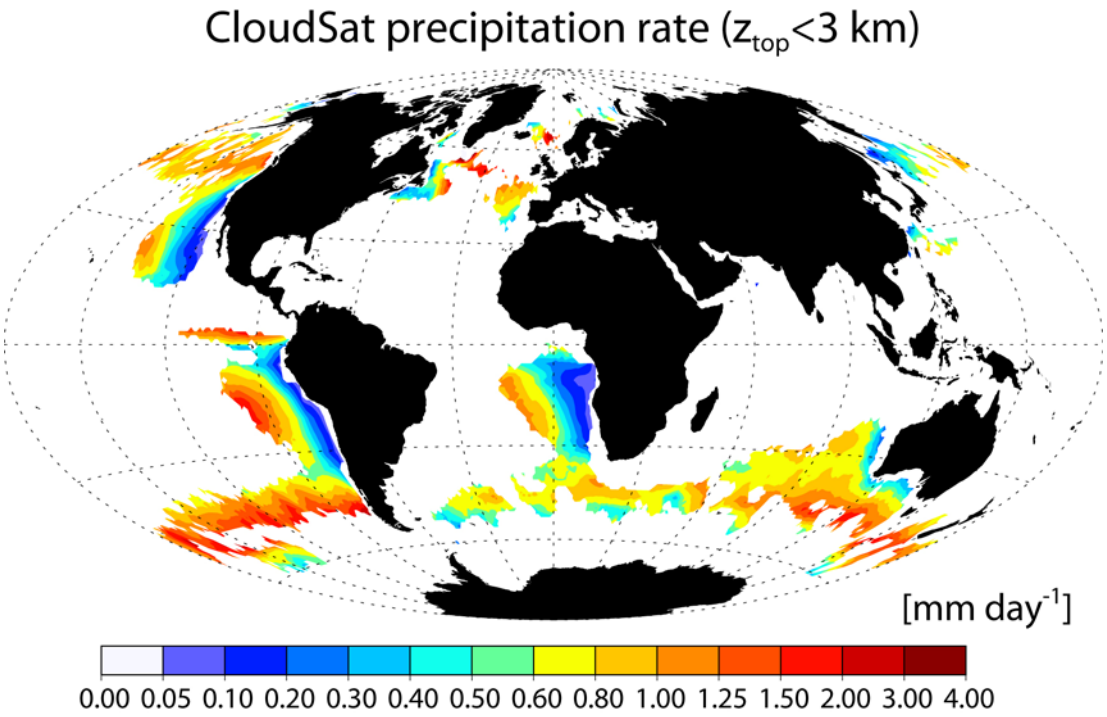

Figure 6: Mean precipitation rate at cloud base from low clouds (cloud top height z_{top}<3 km) estimated with spaceborne radar measurements from CloudSat [Lebsock and L'Ecuyer 2011]**.** Data are screened to display regions of extensive marine low clouds under conditions of mean subsidence as in Fig. 4.

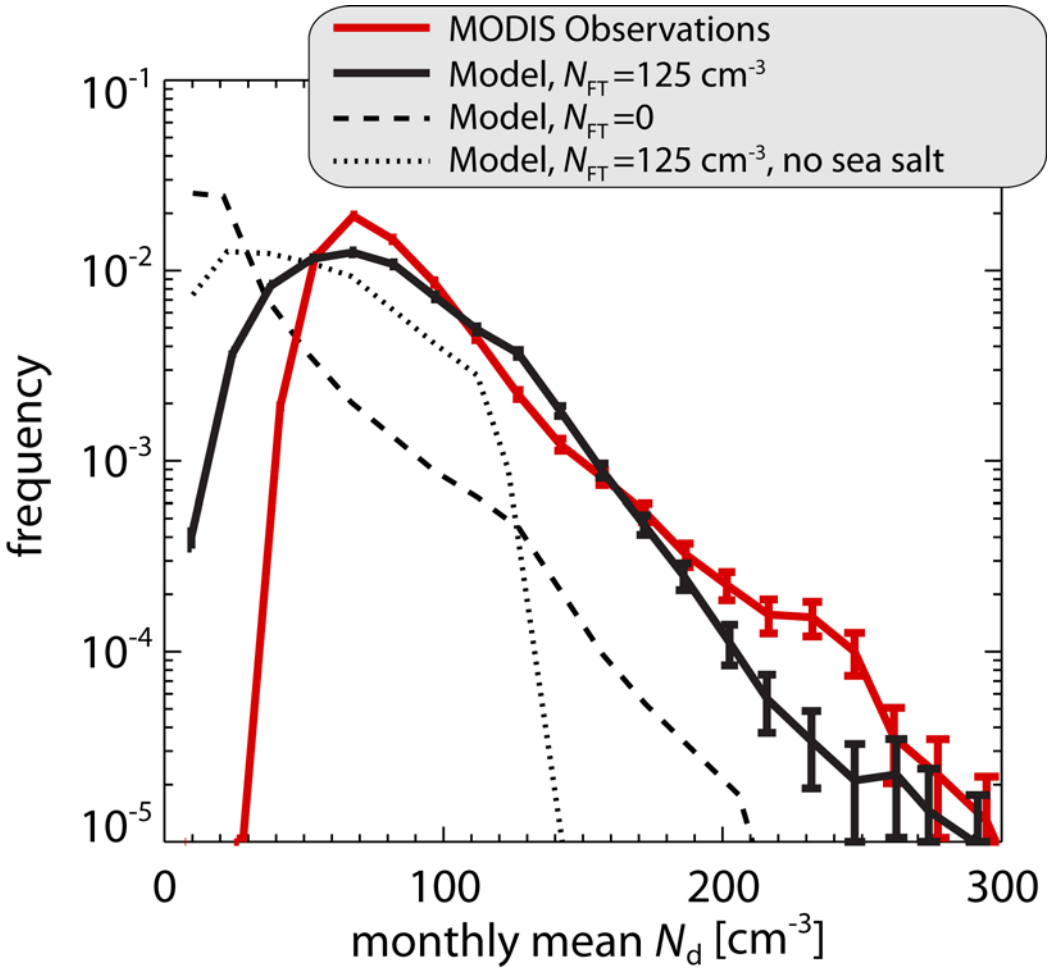

Figure 7: Frequency distributions of observed and modeled monthly mean cloud droplet concentration. Only months that meet the criteria needed to contribute to the means shown in Fig. 4 (regions with extensive low clouds under divergent conditions) are shown. Shown here are the base version of the model (i.e. that used to construct Fig. 4, solid black), together with estimates with no FT contribution to CCN (dashed), and no sea salt contribution (dotted). Error bars show the 95% confidence interval in the frequency estimates for the observations and for the model base case due to sampling limitations.

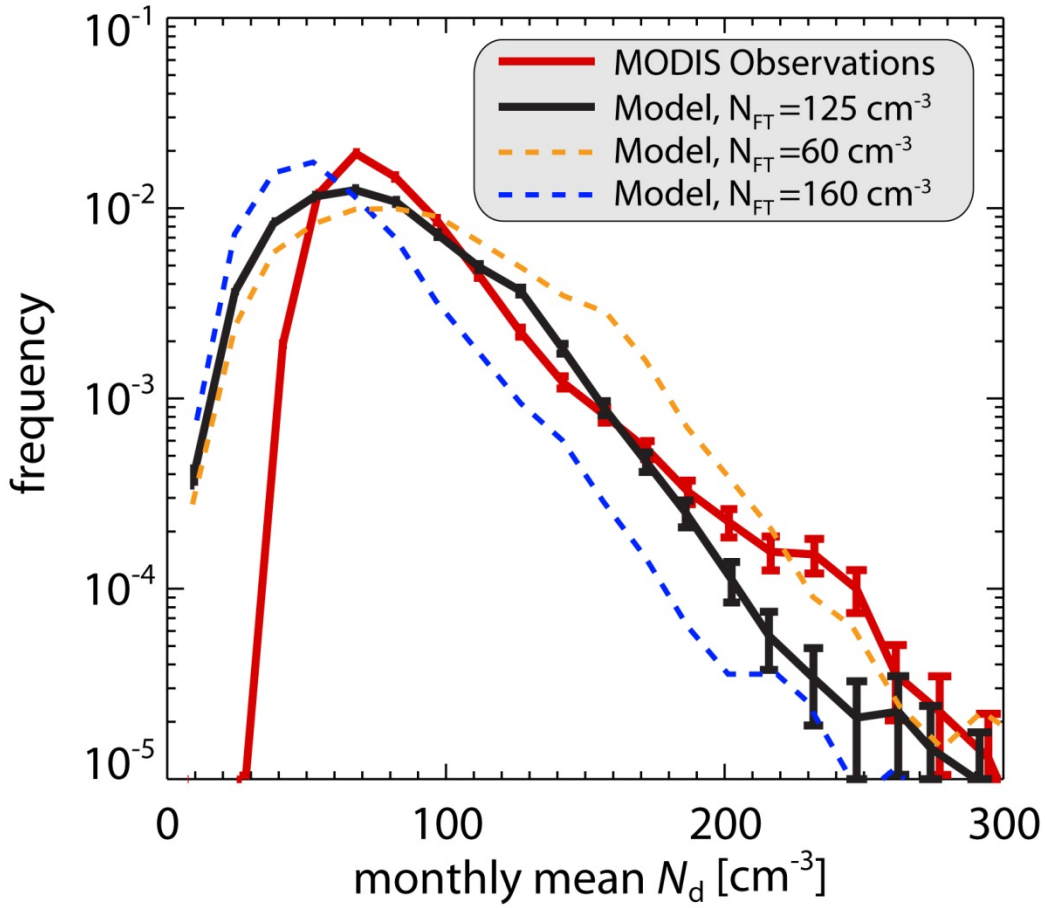

Figure 8: Sensitivity to assumed free tropospheric CCN concentration N_{FT} of the frequency distributions modeled monthly mean cloud droplet concentration. Only months that meet the criteria needed to contribute to the means shown in Fig. 4 (regions with extensive low clouds under divergent conditions) are shown. Shown here are the base version of the model (i.e. that used to construct Fig. 4, solid black), together with model estimates with low (N_{FT} = 80 cm^{-3}) and high (N_{FT} = 160 cm^{-3}) estimates of the FT contribution to CCN (dashed blue and orange respectively). Error bars show the 95% confidence interval in the frequency estimates for the observations and for the model base case due to sampling limitations.